Doctoral Thesis in Solid Mechanics

Modeling the stress-strain response and microstructure development of porous sintered steels

VLADILENA GAISINA

KTH ROYAL INSTITUTE OF TECHNOLOGY

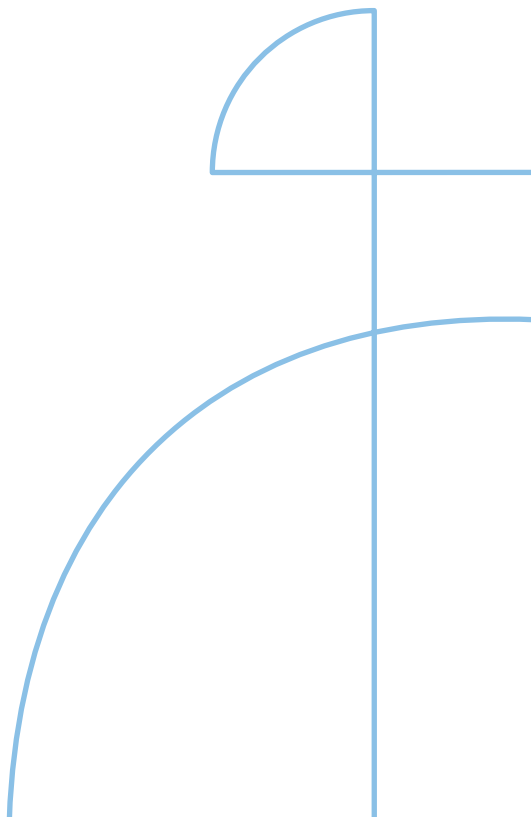

Modeling the stress-strain response and microstructure development of porous sintered steels

VLADILENA GAISINA

Academic Dissertation which, with due permission of the KTH Royal Institute of Technology, is submitted for public defence for the Degree of Doctor of Philosophy on Wednesday the 21st of May 2025, at 1:00 p.m. in F3, Lindstedtvägen 26, Stockholm.

Doctoral Thesis in Solid Mechanics
KTH Royal Institute of Technology
Stockholm, Sweden 2025

© Vladilena Gaisina

TRITA-SCI-FOU 2025:19
ISBN 978-91-8106-245-8

Printed by: Universitetsservice US-AB, Sweden 2025

Only entropy comes easy.

-Anton P. Chekhov

I Abstract

The work in this thesis deals with developing a modeling framework for the prediction of stress-strain behavior and microstructural changes in sintered metals containing porosity. Sintered steels are used in certain structural applications, for example, in the automotive industry. Mechanical behavior then becomes of importance, where compact density plays a major role in controlling properties. In addition, microscale features related to the shape and size of the pores also affect the stress-strain response. These features are, in turn, influenced by the sintering cycle. Thus, a mean-field diffusion-based sintering model is employed together with a representative volume element (RVE) micromechanical model in an attempt to predict experimentally measured properties of a bainitic sintered steel.

Paper A presents a detailed characterization of uniaxial tensile and compressive behavior, based on compact density. Micro and macro hardness testing is carried out and compared with tensile results. Tests on samples of the same green density, subjected to different hold times and temperatures during the sinter cycle, are also performed. Effects of carbon content, pore structure and density on tensile behavior are discussed.

The sintering model is described and presented in Paper B. A new computational framework is introduced for the “two-particle” model, incorporating five different transport mechanisms. Density-dependence is introduced by relating particle overlap to the solid volume in a close-packed structure. Predicted microscopic shrinkage is compared to experimentally measured dimensional change of sintered tensile specimens for two different sinter cycles. A parametric study investigates the influence of different transport

mechanisms and particle size. The quality of fit for the model and reasons for experimentally observed differences between two cycles are discussed.

Micromechanical modeling is addressed in Papers C and D. In Paper C, the RVE is introduced in the form of close-packed overlapping spherical particles. Detailed motivation is given for how the model relates to compact density, microstructural features of the pores and particle size. Matrix parameters are reported, obtained by fitting the experimental tensile curve at one density using small-strain theory and von Mises plasticity. Results are then presented for simulations at five densities, where good agreement is shown between simulated and experimental curves. Lastly, a parametric study investigating the effects of sinter neck curvature is presented.

In Paper D, the RVE is augmented with the introduction of cohesive zones between particles to account for fracture behavior. Cohesive parameters are identified for a bi-linear traction-separation law that give good qualitative agreement between experimental and model results. The effect of varying the number of cohesive zones on the fracture response is investigated. Discussion focuses on further improvements to the model based on *in-situ* microstructural observations found in literature.

In the introduction and conclusion section of the thesis, the proposed framework is discussed in the context of the integrated computational materials engineering (ICME) approach and state of the art in sintering and porosity modeling. Avenues for further development to improve the predictive ability or extend the utility of the model are suggested in the outlook.

Keywords
Powder metallurgy, sintering model, micromechanics, RVE analysis, cohesive zone modeling

II Sammanfattning

Denna avhandling behandlar utveckling av beräkningsmetoder för att förutsäga spännings-töjningsbeteende och mikrostrukturella förändringar i sintrade metaller som innehåller porer. Sintrade stål används i många strukturella tillämpningar, till exempel inom fordonsindustrin. Mekaniska egenskaper blir då av betydelse och densitet spelar en stor roll för att kontrollera dessa egenskaper. De mikroskaliga effekterna, så som storleken och formen på porerna påverkar även spänning-töjningsbeteendet. Dessa egenskaper påverkas i sin tur av sintringscykeln. Således används här en diffusionsmodell baserad på medelfältsteori tillsammans med en mikromekanisk modell med representativ volymelement (RVE) i ett försök att förutsäga experimentellt uppmätta egenskaper hos ett bainitiskt sintrat stål.

Artikel A presenterar en detaljerad karakterisering av enaxligt drag- och kompressionsbeteende, baserat på densitet. Mikro- och makrohårdhetstestning utförs och jämförs med dragprovsresultat. Tester på prover med samma densitet före sintring, utsatta för olika hålltider och temperaturer under sintringscykeln, genomförs också. Effekter av kolhalt, porstruktur och densitet på beteendet vid dragbelastning diskuteras.

Sintringsmodellen beskrivs och presenteras i Artikel B. En ny beräkningsmetod introduceras för "tvåpartikelmodellen", som innefattar fem olika transportmekanismer. Densitetsberoende introduceras genom att relatera partikelöverlappning till volymen i en tätpackad struktur. Simulerad mikroskopisk krympning jämförs med experimentellt uppmätt dimensionsförändring av sintrade dragprover för två olika sintringscykler. Därefter genomfördes en parametrisk studie av effekten av olika

transportmekanismer och partikelstorlek. Noggrannheten hos de numeriska resultaten och orsakerna till experimentellt observerade skillnader mellan två cykler diskuteras också.

Mikromekanisk modellering tas upp i Artiklar C och D. I Artikel C introduceras en RVE-modell i form av tätt packade överlappande sfäriska partiklar. En detaljerad motivering ges för hur modellen beskriver densitet och mikrostrukturella egenskaper hos porerna och partikelstorlek. Konstitutiva parametrar beräknas genom att anpassa den experimentella dragprovkurvan vid en densitet med antagandet om små deformationer och von Mises plasticitet. Med den mikromekaniska modellen beräknades spänning-töjningskurvor vid fem olika densiteten och jämfördes med de experimentella resultaten. God överenstämmelse erhölls. Slutligen presenteras en parametrerstudie som undersökte effekterna av sinterhalsens krökning.

I Artikel D utökas RVE-modellen med införandet av kohesiva zoner mellan partiklar för att beskriva sprickbeteendet mellan partiklar. Kohesiva parametrar identifieras för en bilinjär kohesiv modell som ger god kvalitativ överensstämmelse med experimentella resultat. Effekten av olika antal sammanhängande zoner undersöks. Därefter diskuteras framtida förbättringar av den kohesiva modellen baserat på observationer av mikrostrukturell sprickutveckling presenterat tidigare i andra studier.

I avhandlingens introduktions- och slutsatsavsnitt diskuteras hur den framtagna beräkningsmetoden passar in i ICME-metoden och senaste rön inom sinter- och porositetsmodellering. I avsnittet om möjliga framtida studier föreslås möjligheter för att förbättra prediktionsförmågan och utöka användbarheten av modellen.

Nyckelord
Pulvermetallurgi, sintringsmodell, mikromekanik, RVE-analys, kohesiv zon modellering

III Acknowledgments

This thesis was a project at the Center for Mechanics and Materials Design (MMD), supported by Höganäs AB. I would like to thank MMD for providing this opportunity and gratefully acknowledge Höganäs for their continuous involvement and support during the project.

Furthermore, I am grateful to the supervisory team: Per-Lennart Larsson, Peter Gudmundson, Michael Andersson, Manon Bonvalet and Joakim Odqvist for their leadership and contributions. I would also like to thank Tim Fischer whose collaboration enabled the RVE modelling work in the thesis.

I wish to acknowledge Martin Öberg for his assistance with the experimental work in Paper A, which also provided the basis for mechanical modeling. I am further grateful to my colleagues and professors in Solid Mechanics for sharing their knowledge with me and creating a positive workplace atmosphere. It felt like I had many opportunities for growth, and I am happy to be part of the KTH Solid Mechanics network.

I appreciated, as well, sharing the experience with other PhD students in MMD. It was nice to have another community in addition to my own program.

Lastly, I wish to express my warmest gratitude to my friends and loved ones for their continuous support, from near and far. And to all the mentors who believed in and encouraged me – thank you for everything.

IV List of publications

Appended papers

Paper A – V. Gaisina, M. Andersson, M. Bonvalet-Rolland, J. Odqvist, P.-L. Larsson, and P. Gudmundson (2022) "On the mechanical behavior of sintered Astaloy-85Mo: Influence of porosity and sinter conditions," *Materials Science and Engineering: A,* vol. 841, p. 143052.

Paper B – V. Gaisina, M. B. Rolland, M. Andersson, P.-L. Larsson, and P. Gudmundson (2024) "Modeling neck evolution and shrinkage during sintering of Astaloy® 85 Mo," *Computational Particle Mechanics,* published online.

Paper C – T. Fischer, V. Gaisina, M. Andersson, P.-L. Larsson, and P. Gudmundson (2024) "Micromechanical prediction of the elastic and plastic properties of sintered steels," *Materials Science and Engineering: A,* vol. 897.

Paper D – V. Gaisina, T. Fischer, M. Andersson, P.-L. Larsson, and P. Gudmundson, "Micromechanical modeling of density-dependent fracture in porous sintered steel") Submitted for international publication.

Author contributions

The thesis author's contribution to the appended papers, according to CRediT (Contribution Roles Taxonomy):

Paper A	Data curation, Formal analysis, Investigation, Visualization, Writing – original draft, Writing – review & editing
Paper B	Conceptualization, Data curation, Investigation, Software, Validation, Visualization, Writing – original draft, Writing – review & editing
Paper C	Conceptualization, Data curation, Investigation, Writing – original draft, Writing – review & editing
Paper D	Conceptualization, Data curation, Formal analysis, Investigation, Methodology, Software, Visualization, Writing – original draft, Writing – review & editing

Contributions from other authors are detailed at the end of the respective papers.

V Scientific work not included in the thesis

Conference paper

V. Gaisina, M. Bonvalet-Rolland, M. Andersson, J. Odqvist, P.-L. Larsson, and P. Gudmundson (2020) ”An experimental investigation of the mechanical behavior of sintered Astaloy™ 85 Mo,” EP2004849263 In: *Proceedings – Euro PM2020 Congress and Exhibition*, European Powder Metallurgy Association (EPMA).

VI List of abbreviations

CZM	Cohesive zone modeling
DC	Dimensional change
DEM	Discrete element method
FCC	Face-centered cubic
FE	Finite element
GTN	Gurson-Tvergaard-Needleman
ICME	Integrated computational materials engineering
kMC	Kinetic Monte-Carlo
MD	Molecular dynamics
MIM	Metal injection molding
PBC	Periodic boundary conditions
PM	Powder metallurgy
PSD	Particle size distribution
PSPP	Process-structure-properties-performance
R.d.	Relative density
RVE	Representative volume element
SDC	System design chart

UTS	Ultimate tensile strength
Wt	Weight

CONTENTS

List of Figures

List of Tables

1 Introduction

1.1 Motivation

Pressing and sintering of steels has grown in industrial importance in the second half of the 20th century as a versatile and cost-efficient method of manufacturing complex and precise geometry parts at scale [1]. Historically, technological innovation in this area has advanced faster than modeling capabilities. This is due in part to the varied porous microstructure inherent in this class of materials. The process chain is designed to optimize for geometric precision rather than full densification, meaning that the voids remaining after the densification process are still present at the end of the sintering cycle. Moreover, while some rounding is observed in the pore corners, they remain largely irregular in shape, differing in size and distribution [2, 3]. Thus, it is important to understand the impact of porosity, formed during the process chain, on the mechanical properties of sintered steels.

1.2 Scope and objectives

At the core of this thesis is the development of a tool to predict mechanical properties of sintered steels containing porosity. To this end, several objectives are pertinent:

- Understanding how processing parameters like compact density as well as sintering time and temperature affect the mechanical properties of a given steel (Paper A).
- Developing a suitable model for the sintering process that would capture relevant microstructural changes due to initial density and sinter cycle (Paper B).

- Developing a micromechanical model that would capture the density-dependent mechanical behavior of sintered steel and consider microstructural aspects of pore shape (Papers C and D).

Sintered steels are influenced by many processing and material factors from the powder production stage to the sintering stage. To limit the modeling work to a manageable scope, the focus of this thesis is placed on accounting for compact density, porosity characteristics, and, to a lesser extent, sintering cycle and some powder properties. Much academic work has been carried out within the subjects of sintering and property modeling of porous materials [4-7]. The approach in this work relies on bridging of the two subjects in order to predict mechanical behavior, grounded in micromechanics and experiments.

To validate the modeling approach with experimental data, the investigation in this work has concerned a single material, Astaloy® 85 Mo, a water-atomized iron powder pre-alloyed with 0.85 wt % molybdenum, with 0.4 wt % or 0.6 wt % carbon added for strength. To ensure the model would be suitable for commercial sintered steels, typical commercial powder was used, with the test samples manufactured by Höganäs AB according to a typical industrial process that would be representative for a sintered component. The cooling rate was selected to produce a mostly fully bainitic microstructure.

Thus, the objective of this thesis has been the development of a modeling framework that considers the influence of complex pore shape and sinter cycle on the stress-strain behavior of real powder compacts.

2 Background

2.1 Powder metal and sintered steels

Metal powder can be processed in many ways to form a product; in the case of press and sinter, the core operations are a compaction and a sintering step. The primary advantage of a powder-form starting material is the shape complexity and close tolerances that can be achieved with fewer processing steps and high material utilization [1]. The powder mix before compaction has liquid-like flow properties at room temperature, making it easier to handle and offering better surface finish as compared to casting processes. The secondary advantage of powder-based materials is an alternative approach to alloying, as well as the ability to create composite materials with constituents that have little affinity in their liquid state. However, due to the cost of the dies used for powder compaction, a certain production volume should be reached for the powder metallurgy (PM) processes to become economically advantageous. Another limitation is the size of the component, since the compaction forces required scale with compaction area. Lastly, the geometry of the part must be such that it is possible to form and eject from the mold with uniaxial die movement.

Since PM processes are particularly well-suited for the mass production of smaller complex-shaped parts with close tolerances, common products include gears, cams, hubs, bearings, as well as soft magnets and filters. Typical structural applications where steel powder is likely to be used are found in the automotive industry, home appliances, office machines and power tools.

A unique aspect of powder steels produced by pressing and sintering is that density is an important factor that controls the mechanical properties (as opposed to wrought or cast materials where the desired properties are achieved

by thermo-mechanical treatments). This is also in contrast to other powder metal processes designed to reach almost full density (*e.g.* metal injection molding (MIM) or liquid phase sintering). For commercial steels, such as Astaloy® 85Mo, the density controlling step is the powder compaction. On the macro scale, compaction produces a green body conforming to the shape of the part, while on the micro scale this causes rearrangement and some deformation of the particles, where flat contact surfaces are formed. These "cold-welded" contacts develop into interparticle necks during the subsequent sintering step. While some shrinkage of the compact is expected to occur during sintering due to atomic diffusion, it is on the order of tenths of a percent rather than tens of percent. Despite this minor change, a ten- to twenty-fold increase in mechanical strength is observed between the green body and the fully sintered part. This indicates there are important micro-scale features controlling mechanical properties besides macroscopic density: the size of interparticle necks formed at the interface of deformed particles and changes to porosity characteristics during sintering. Thus, it is insufficient to consider density as a single parameter when attempting to model this type of material.

2.2 ICME approach

In order to design better materials, improve on the existing ones or understand material behavior, a useful approach is through the lens of Integrated Computational Materials Engineering (ICME) [8]. A widely-used tool within ICME is a system design chart, also known as a process-structure-properties-performance (PSPP) map. As the name suggests, it consists of three columns, one for the particular manufacturing process employed, one for the microstructural features in the material, and one for properties of interest. The known or suspected linkages between the sub-units in different columns are drawn with solid or dashed lines. This representation offers a way to visualize not only the entire process chain, but also the hierarchy of microstructural components, as well as the interconnections between a) individual processing steps and microstructure and b) microstructural features and the physical properties of interest. In structural applications, these properties are often strength, stiffness and fatigue limit.

Another core feature of ICME, then, is computational modeling. If each linkage in an SDC represents a connection between two things, it should be possible to incorporate this relationship into a model. It's important to remember that said models may be empirical, which are typically easier to derive but are

interpolative in nature, physical, stochastic, or a combination of the above. The goal is always to increase the predictive ability of the computational models used, as this is what truly allows for computationally powered materials design or development. Since the linkages are often complex, *e.g.* with many processing steps contributing to a given structural feature, the models can simultaneously incorporate several dependencies across different length and time scales.

The system design chart can thus be used as either a design tool, with which changes to the material processing can be proposed, computed to achieve the desired properties through optimized microstructure, or an exploration tool to better understand and quantify what gives a material certain properties. Since the motivation behind this work is to develop a predictive tool for the mechanical properties of sintered steels containing porosity, the ICME framework is a useful approach.

The manufacturing process for the material investigated in this work follows closely a typical PM process [1], captured on Figure 1. Figure 1 shows a system design chart for a generic sintered steel, produced from either sponge iron or pre-alloyed powder. The dashed boxes show optional steps, such as diffusion alloying (during the sintering process) and surface treatments (for example, carburizing). It is worth noting that the material used for experiments and investigated in this work is in its as-sintered state, in order to reduce the complexity of the system and focus primarily on the effect of pores on properties. The simplified chart for Astaloy® 85 Mo + C applicable to this work is then shown in Figure 2.

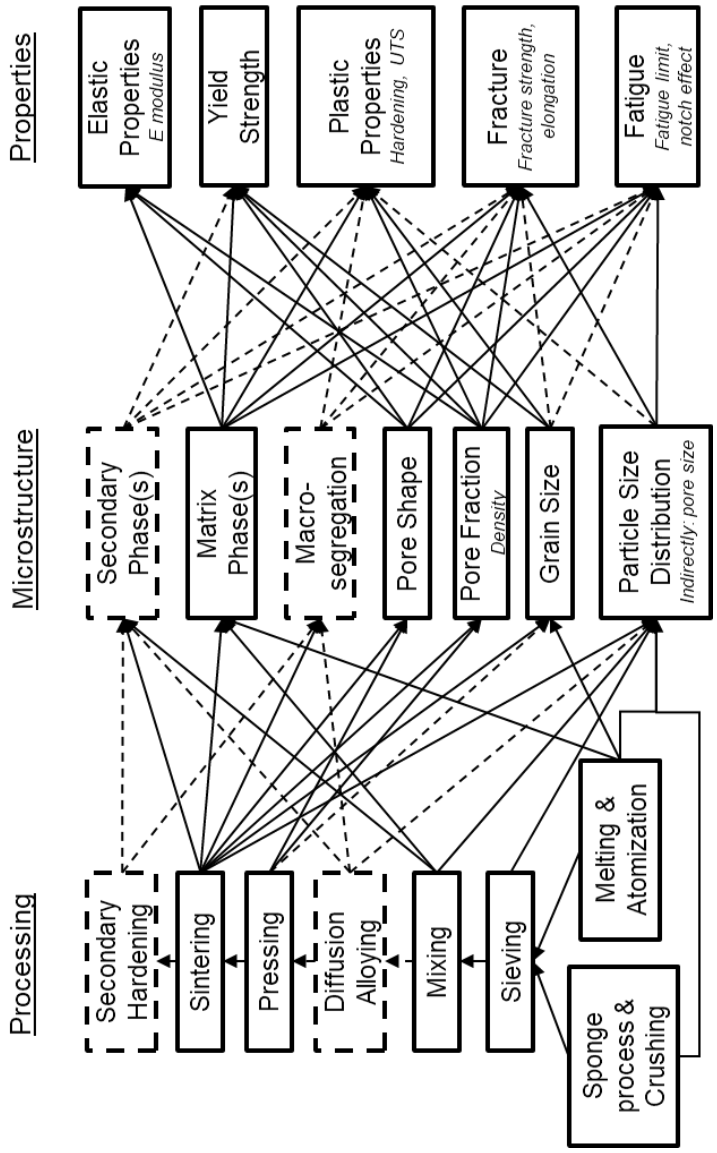

Figure 1: System Design Chart for a generic press-and-sinter steel.

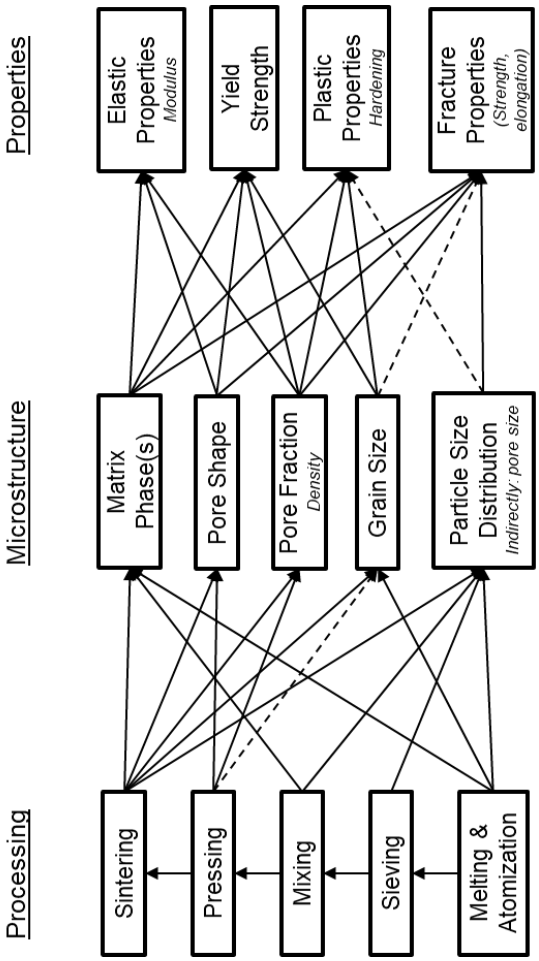

Figure 2: System Design Chart for the material used in this thesis work, Astaloy® 85 Mo with 0.4%-0.6% graphite addition.

The major factors controlling the mechanical properties of sintered steels are:

- Composition
- Powder size and size distribution
- Compact density
- Sinter cycle (heating rate, time, temperature, atmosphere, cooling)

Some of these affect primarily porosity, some primarily the matrix material, and some both (as can be observed in detail by studying the linkages on Figure 1 and

Figure 2). Due to a locally non-uniform microstructure, there is an inherent statistical aspect in describing both the microstructure and mechanical properties. The simplest approach in this case is to model an averaged representation. As this work demonstrates, such an approach can be successfully adapted when the influential factors described above are effectively captured by the model.

2.3 Porous material modeling

The fundamental question in modeling sintered metals is whether to treat them as porous continua or as connected particles. Analyses of void growth in ductile materials have been carried out over decades of research, with seminal contributions made by Rice and Tracey [9], Gurson [10] and Tvergaard [11]. Further efforts included work in void coalescence [12, 13] and the introduction of a length scale [14, 15]. Various modifications have been proposed to the Gurson-Tvergaard-Needleman (GTN) model in the context of modeling sintered iron and steel [16-18]. However, such models have proven to have limited predictive capabilities for density dependence in these materials at higher porosity levels (~>5-6%), requiring parameter fitting for each material. The same holds for classical results derived by Eshelby [19] for elastic properties of porous metals.

It has also been demonstrated that sintered steels are generally more brittle than wrought metals of similar strength [20]. In fact, many sintered steels used in structural applications (including the one investigated in this work) exhibit quasi-brittle fracture characteristics (see Figure 3). This is not consistent with the assumptions of ductile crack growth associated with the GTN model, commonly used with other metallic materials. This suggests that the physical mechanisms behind damage evolution in PM materials are fundamentally different. Thus, it is worth exploring if particle-scale models would give a more physical description. Indeed, experimental investigations have shown that local microstructure (such as the shape, size and proximity of voids) and associated deformation behavior control macroscopic properties [21-24].

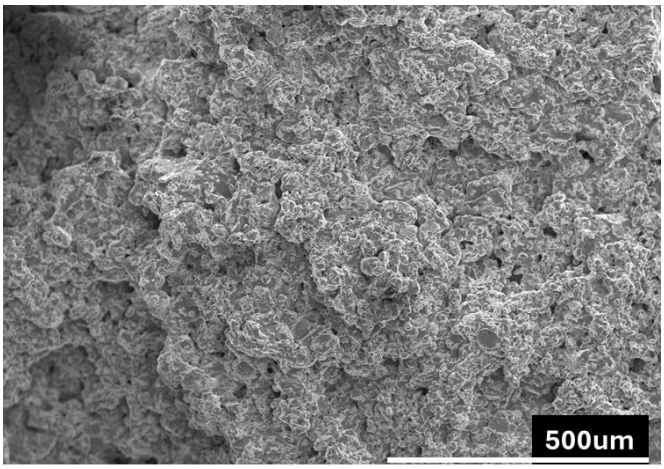

Figure 3: Tensile fracture surface of an 89.3% r.d. sample showing quasi-brittle characteristics.

The particle-based approach can also be justified within the ICME context, where multi-scale modeling linking processing, structure and properties is of interest. The constitutive parameters in porous continuum models described above are material constants not connected to quantifiable pore characteristics. By contrast, various sintering models have been developed at the particle scale, which relate to pore geometry. More background to this is given in the next section.

2.4 Sintering modeling

Modeling the sintering process is a vast and mature field, taking shape in the second half of the 20th century and encompassing both metal and ceramics sintering. For the purposes of this work, the methods applicable to particle-scale simulations are in focus. Such methods can be broadly divided into two categories:

1. Geometry-agnostic methods that do not contain any assumptions on the particle shape and therfore can be freely applied to any initial particle shape or arrangement.
2. Geometry-specific methods, where the evolutive equations themslves are derived based on a specific geometry of the particles and neck. In most cases, the particles are represented by perfect spheres.

In the first category, at the smallest scale of physical models, molecular dynamics (MD), which tracks the paths of individual atoms, can be used to study the sintering of nanoparticles [25]. Mesoscale methods include phase-field [26,

27] and kinetic Monte-Carlo (kMC) [28, 29]. In both cases, a compromise must be made between computational time and level of detail. In this respect, kMC may be more efficient, but as a statistical mechanics method it does not inherently incorporate any thermodynamic quantities and thus a challenge arises in making it specific to the material system of interest. Some authors have shown how kMC could be adopted into a multi-scale modeling framework [29, 30].

The second category comprises such approaches as the "two-particle" method, where the geometrical changes in two spherical particles joined by a sinter neck are described with analytical expressions. Material-specific diffusion properties are in this case incorporated into flux equations for each of the possible transport pathways [31, 32]. Svoboda & Riedel [33] proposed a description incorporating macroscopic stress for pressure-assisted sintering, later built upon by Bouvard & McMeeking [34, 35]. These authors have adopted thermodynamic descriptions into a mechanical framework of discrete elements (DEM) to further extend the model to rows of particles and 3-D assemblies [35, 36]. These methods offer the advantage of containing kinetic material parameters in the form which can be directly taken from literature or thermodynamic databases. Because the discretization in this case is at the particle level, they are also more computationally efficient. On the other hand, the geometric assumptions they are built upon are inherently simplified as compared to real microstructures.

3 Mean-field sintering model (Process-Structure)

3.1 Background

In principle, most of the models described in Section 2.4 could be suitable for carrying out the objectives of this thesis. Considering the particle size of the powder investigated in this work is on the scale of ~100 μm, a mesoscale method would be most appropriate. From a predictive standpoint, the models that incorporate mobility data are also most promising, as such models could draw from computational thermodynamic data to readily consider the effect of composition, time and temperature in sintering. On the other hand, consideration must be given to connecting the results of the sintering model to the mechanical model.

The proposed mean-field approach is particularly well-suited for the material at hand and has several advantages in this application over other sinter models. As compared to kMC, for example, it has easy coupling with thermodynamic and kinetic databases through its transport equations, making it adaptable to multicomponent and multiphase materials. With regards to other physical models, such as MD and phase-field, it cannot handle local geometrical effects (such as groove angle) with high fidelity, as it relies on assumptions of a simplified geometry. However, the mean-field model is not limited by system size and can be used to describe macroscopic behavior of a material containing a high number of particles.

3.2 Method

The present work proposes a mathematical framework for evaluating the geometrical changes for a system of equisized spherical particles, resulting from the main transport mechanisms active in solid-state diffusion. The model is derived for a primary system of two particles connected by an interparticle neck. The number of contacts at each particle can be incorporated to account for neck growth at all contact surfaces. Similar approaches have been used elsewhere in literature, for example by Xu, et al. [21], Pan et al. [13], German and Hwang [19]. The present work differs in several key areas: first, a simplified computational scheme is introduced with an analytically derived relationship between initial density and center-to-center particle distance for an assumed ideal packing; and second, the model is coupled with mobility data obtained from Thermo-Calc [34] to demonstrate feasibility of building an integrated computational mean-field model capable of extracting data from thermodynamic and kinetic databases to make microstructure and property predictions.

To allow for the formation and growth of the neck, multiple transport mechanisms act simultaneously to enable atomic migration from the particles' surface or bulk toward this neck. This includes [36]: (i) diffusion over the surface to the neck (SD), (ii) volume diffusion through the bulk from particle surface to the neck (VA), (iii) evaporation of atoms from the surface and condensation at the neck (EC), (iv) diffusion along the interior grain boundary toward the neck surface (GB), and (v) volume diffusion from the contact area (VD), all depicted in Figure 4.

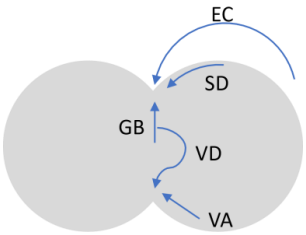

Figure 4: A schematic illustration of the sintering mechanisms considered in the model. GB denotes grain boundary diffusion, SD is surface diffusion, EC is evaporation and condensation, while VA and VD are volume diffusion originating either from particle surface or the grain boundary.

Figure 5(a) illustrates the geometrical parameters of two overlapping particles, taken as a basis for the derivation. The full model considers N number of contacts per particle. Here the particle radius is denoted by R, center-to-center distance is $2L$, the size or radius of the interparticle neck formed during sintering

is x, while the neck curvature radius is r, and angle β is taken as the angle from the central axis of the neck to the edge of the connected particle. Finally, the neck volume is denoted as V_{n} and the volume of the overlapping boundary as V_{b}. Conservation of mass dictates that the volume lost due to particles drawing closer together (V_{b}), as well as due to atoms diffusing away from particle surface (V_{s}), must together equal the volume increase at the neck (V_{n}).

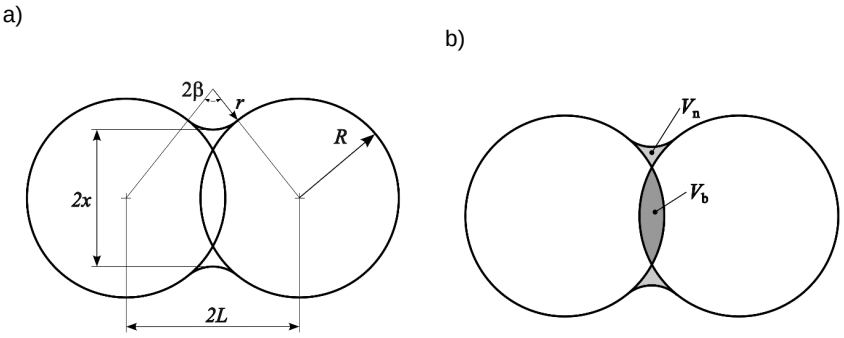

Figure 5: Schematic diagrams showing the two-sphere sintering model with specified geometric variables. a) Geometric variables pertaining to the particles and neck. b) Illustration of the volume lost from sphere overlap, V_b, and the total neck volume, V_n. Not shown is the volume lost from the surface of the spheres, V_s.

Full details of the derivation and governing equations are given in Paper B. Figure 6 shows a schematic depiction of model functionality. The appended Paper B also contains a table of parameters used in the work. It bears mention that surface diffusion and grain boundary diffusion coefficients were taken from literature, as Thermo-Calc only provides data for volume diffusion. The optimization of coefficients to fit the experiments is left for future work, while the focus of this study was placed on qualitatively capturing time and temperature dependence and investigating particle size effects.

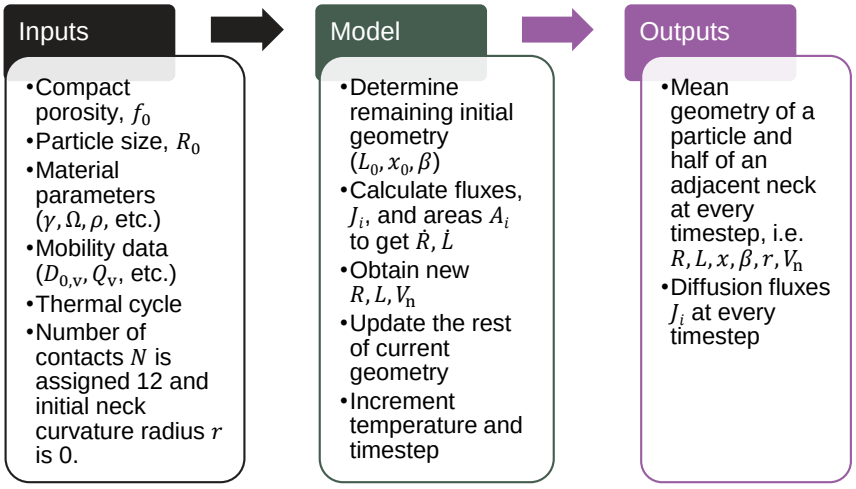

Figure 6: Schematic of model inputs, outputs, and operations.

3.3 Experimental and modeled results

The previously described model was applied to Astaloy® 85 Mo tensile samples admixed with 0.6 wt. % graphite, pressed up to four different densities and sintered at different sinter cycles in low-pressure atmosphere consisting of 90% N_2 and 10% H_2 inside a batch furnace. The dimensional change in the length of the tensile bars before and after sintering was compared with model predictions.

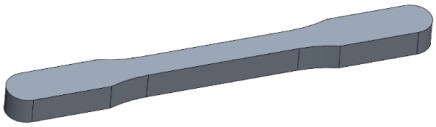

Figure 7: Tensile samples, measuring 90 mm in length, used to provide experimental shrinkage measurements in this study.

The absolute and relative ("r.d.") sintered densities for each batch are shown in Table 1. Density measurements were performed by Archimedes method. To capture the effect of time and temperature, two different hold temperatures and two different hold times during the sintering cycle were used in this work. The full process matrix is presented in Table 1 below.

Cycle	Sintered density (g/cm³) (relative density)			
	"6.5"	**"6.8"**	**"7.0"**	**"7.2"**
1120 °C / 15 min		6.8 (0.87)	7.02 (0.89)	7.23 (0.92)
1120 °C / 30 min	6.49 (0.83)	6.81 (0.87)	7.02 (0.89)	7.25 (0.92)
1250 °C / 30 min	6.62 (0.84)	6.88 (0.88)	7.08 (0.90)	7.30 (0.93)

Table 1: Measured sample densities post-sinter for each sinter cycle performed.

To compare model predictions with experiments, the change in center-to-center distance ($\Delta L/L_0$, see Figure 5(a)) is plotted against the measured macroscopic dimensional change (DC) in Figure 8 and Figure 9. Model predictions were made for each of the relative densities measured, plus two extra points to illustrate overall behavior.

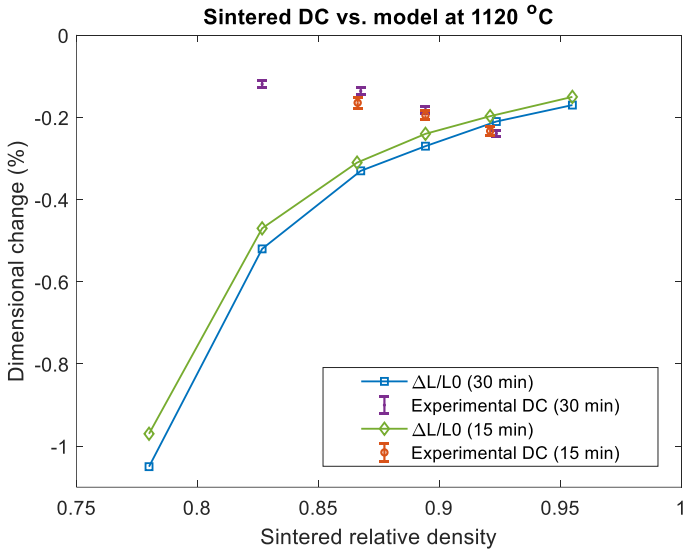

Figure 8: Predicted measures of linear dimensional change (lines with markers) compared with experimentally measured dimensional change (markers with error bars) in test compacts for "1120 °C / 30 min" and "1120°C / 15 min" cycles.

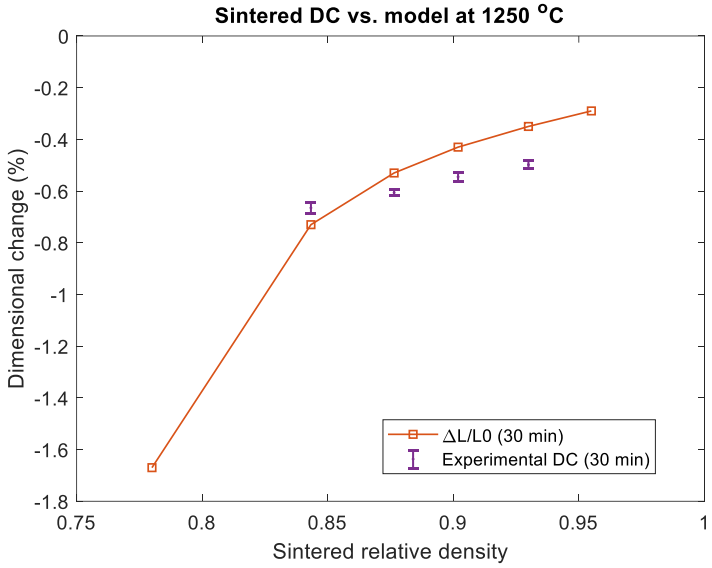

Figure 9: Predicted measures of linear dimensional change (line with markers) compared with experimentally measured dimensional change (markers with error bars) in test compacts for "1250 °C / 30 min" cycle.

Notably, the experimental trends in the dimensional change with density appear to be different between the two temperatures, which has also been confirmed by repeat experiments. Meanwhile, the model predictions have the same trend for both, which is in line with sintering theory for regularly packed spherical particles [37]. The flux parameter investigation in Paper B offers a possible explanation for this.

When changes in geometry were investigated for the 1120°C / 30 min cycle in Paper B by assessing the effect of different transport mechanisms, it was demonstrated that boundary diffusion (GB) promoted linear shrinkage $\Delta L/L_0$, while the absence of surface diffusion (SD) also led to higher shrinkage. Consequently, it is possible that lower shrinkage is seen at lower densities because more transport effects occur due to surface diffusion. Since the thermal history of different density samples is identical, there must be something about the physical particles or their arrangement that is responsible for this. As opposed to the model description, the real particles are not ideally spherical and possess surface topology features as a result of the water atomization process. At lower densities, fewer particle contacts are formed, meaning more of the original surface remains. Sintering lowers the surface energy of the system by reducing the surface area and curvature via mass transport events. This would

result in smoothing and spheroidizing of the particle surface. Thus, it is likely that surface diffusion dominates the early stages of sintering, but boundary diffusion becomes more significant at higher temperatures, as can be deduced from Figure 9.

A parametric study on the effect of initial particle size on linear shrinkage ($\Delta L/L_0$) was performed and plotted together with the experimental DC measurements for the 1120°C / 30 min cycle (Figure 10).

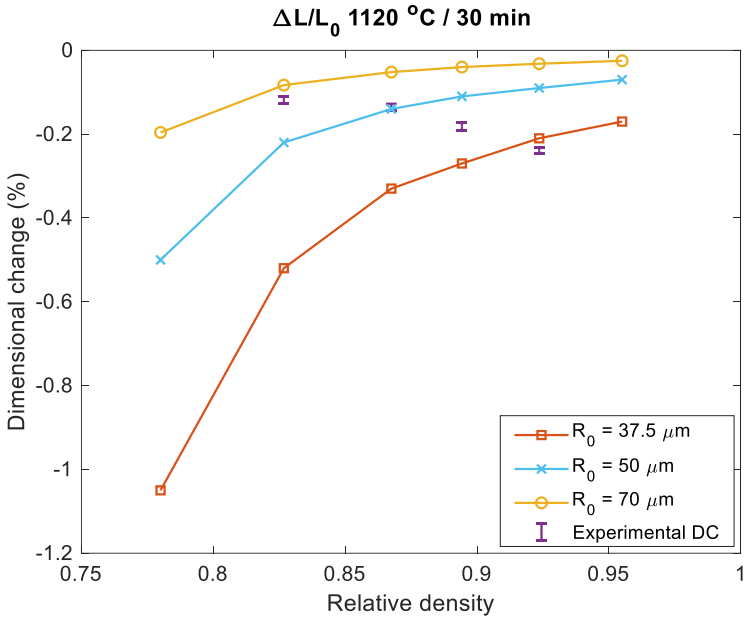

Figure 10: Effect of initial particle size on model predictions of linear shrinkage for "1120 °C / 30 min" cycle, plotted with experimental DC measurements.

In line with sintering theory and practical observations, increasing particle size decreases the total amount of shrinkage at every density. This study shows a drastic effect of particle size at the lower densities and a lesser sensitivity to powder size at the higher densities (with the caveat that the model does not capture the experimental trend at 1120°C for this material). This suggests higher density contacts are less sensitive to variations in particle size distribution (PSD). In addition, this illustrates how the mean-field model could potentially be adapted to incorporating a distribution of particle sizes by simulating multiple diameters and applying a weight function to the results, based on known PSD.

4 Micromechanical RVE model (Structure-Properties)

4.1 Background

The basis for the mechanical model in this work was the consideration of a more representative microstructure. Early finite element (FE) simulations in this area were pioneered by Bourcier *et al.* [38], who investigated microcells with oblate cavities. Becker [39] considered heterogeneous porosity distributions in an axisymmetric model of iron compacts with up to 6% porosity.

More recent seminal work has been carried out by Chawla and Deng [21] by performing 2D simulations on a meshed section reproduced from a micrograph. Andersson and Schneider took it a step further in simulating the effect of density on stress-strain curves using reconstructed and generated 2D meshes [40, 41]. Fritzen *et al.* [17] used 3D RVE models to consider heterogeneous spherical pore distributions in elasto-plastic metals. Nagata *et al.* [42] took the approach of introducing void elements in a fine square mesh of an elastic gear tooth. Other authors have relied on X-ray microtomography for microstructure-based numerical modeling of a different material at higher porosity levels than the porous steel studied here [43].

The studies described above have either targeted precise reproduction of physical microstructures or, on the other hand, adopted simplified spherical or oblate pore geometries. The approach in this work strikes a middle ground by considering a unit cell assembly of overlapping spherical particles, forming pores with sharp features. This approach offers certain advantages over other microstructure-based methods, as will be discussed in the following section.

4.2 Method

Paper C first introduces the model with an elasto-plastic material implementation. In Paper D, the model is extended to fracture with the addition of cohesive zones. A brief description of the RVE model is given here.

The porous microstructure of the material is represented by a 3D face-centered cubic (fcc) unit cell, illustrated in Figure 11. Each particle is 100 μm in diameter. The desired density in the RVE is achieved by changing the degree of particle overlap - as observed in the RVE, the degree of particle overlap reduces the pore volume, thus controlling prescribed density. The contacts between particles represent sinter necks and are constructed with cohesive elements. A small radius at the contact edge corresponds to the neck radius in the sinter model, thus incorporating the effects of the sintering step where neck growth and rounding occur. In total, there are 24 particle bonds.

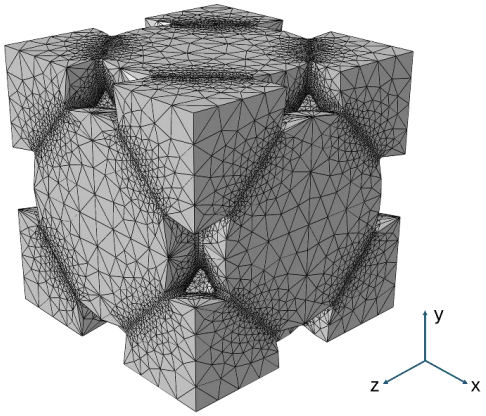

Figure 11: Full view of the RVE with mesh refinement at particle contacts.

An adaptive mesh that is refined near the sintered necks and coarsened away from these regions enables a balance between computational accuracy with efficiency. The fine mesh at the necks is employed to accurately capture the stresses and strains in geometrically complex regions. Mesh continuity on opposite faces enables the application of periodic boundary conditions (PBCs) in all directions. This approach reproduces a macroscopic uniaxial stress state that aligns with experimental tensile test conditions. Under quasi-static loading, the RVE is axially displaced in the *z*-direction until the desired macroscopic strain is reached.

The constitutive behavior of the matrix material is modeled using the classical approach for metallic materials, comprising isotropic elasticity and von Mises plasticity, under the assumption of small strains. The hardening behavior is described using Voce's power law:

$$\sigma = \sigma_0 + (\sigma_\infty - \sigma_0)\left[1 - \exp\left(-b\varepsilon_{\mathrm{p}}\right)\right], \tag{1}$$

where σ_0 represents the initial yield stress, σ_∞ is the saturation stress in the exponential approximation, and b is a material constant.

The model parameters in Table 2 were obtained by fitting the RVE response at one particular density to the experimental curve. As demonstrated in Paper C, this results in good agreement of simulated behavior with experiments at the other densities.

E, GPa	ν, -	σ_0, MPa	σ_∞, MPa	b, -
198	0.3	420	640	80

Table 2: Constitutive parameters used in the model.

The cohesive elements implemented in this model are the standard COH3D6 wedge elements in Abaqus (2019) with element removal activated. Quadratic nominal stress criterion (QUADS) (2019) was selected as the damage initiation criterion, described by

$$\left\{\frac{\langle t_{\mathrm{n}}\rangle}{t_{\mathrm{c,n}}}\right\}^2 + \left\{\frac{t_{\mathrm{s}}}{t_{\mathrm{c,s}}}\right\}^2 + \left\{\frac{t_{\mathrm{t}}}{t_{\mathrm{c,s}}}\right\}^2 = 1\,, \tag{2}$$

where t_{c} is the peak value of the nominal stress corresponding to deformation in the purely normal to the interface direction or purely to the first and second shear directions, as denoted by the subscripts n, t, and s, respectively. In this work, the same critical value is taken for both shear directions.

The damage evolution, in turn, is dictated by a power-law fracture criterion for mixed-mode conditions as

$$\left\{\frac{G_{\mathrm{n}}}{G_{\mathrm{c,n}}}\right\}^\alpha + \left\{\frac{G_{\mathrm{s}}}{G_{\mathrm{c,s}}}\right\}^\alpha + \left\{\frac{G_{\mathrm{t}}}{G_{\mathrm{c,s}}}\right\}^\alpha = 1\,. \tag{3}$$

Here, G_{c} is the energy required to cause failure in the individual modes (following the same notation convention as (2)), while G_{n}, G_{s} and G_{t} denote the work done by the tractions and the conjugate relative displacements in the three directions as described above. In this work, the coefficient α is set to 1. Parameter values corresponding to the variables in equations 2 and 3 are given in Table 3 and were obtained by fitting the simulated curves to the experimental results in

a similar manner as the matrix constitutive parameters. In Table 3, "k" denotes the initial stiffness parameter and δ_f the separation distance in the bilinear traction-separation description governing the cohesive response. An illustration of this is shown in Paper D.

Normal direction				*Shear directions*			
k (GPa/m)	$t_{c,n}$ (MPa)	$G_{c,n}$ (J/m²)	δ_f (μm)	k (GPa/m)	$t_{c,s}$ (MPa)	$G_{c,s}$ (J/m²)	δ_f (μm)
1.77E8	1450	113	0.16	1.77E8	1600	141	0.18

Table 3: Cohesive parameters used in the model for particle radius 100 μm.

4.3 Experimental and modeled results

The simulation results are then shown in Figure 12, where fully modeled curves are plotted for all five densities. Both the matrix and cohesive parameters were calibrated for only one density. The curves designated "NoCOH" refer to models without any cohesive zones, set to terminate at a strain value corresponding to the average fracture strain from experiments. By contrast, curves where a cohesive layer is present at all necks are designated "COH" and terminate when the simulation reaches non-convergence. These results verify that the addition of cohesive zones and their respective parameters has not significantly altered the elastic and hardening behavior calibrated previously.

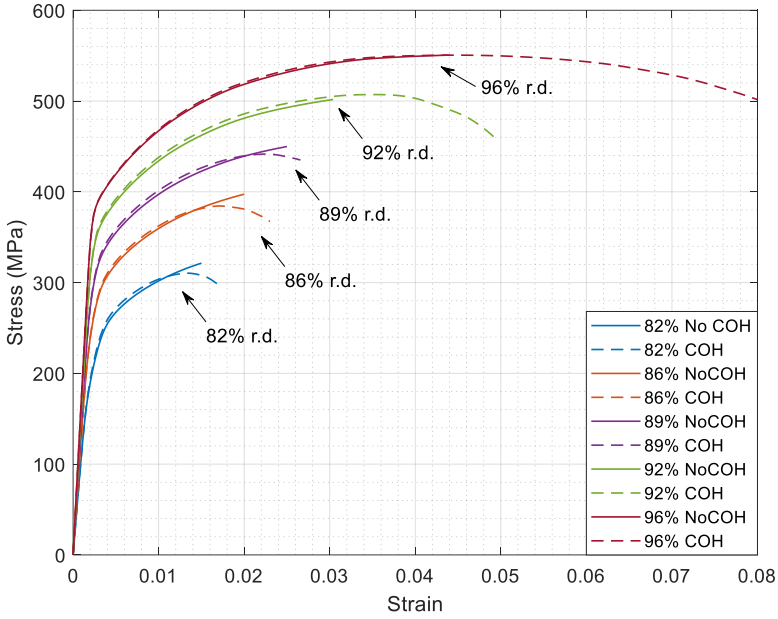

Figure 12: Effect of adding cohesive zones to the RVE model. Simulation results are shown for each density for a model with no cohesive zones ("No COH") and one where all sinter necks have a cohesive layer ("COH"). Curves with cohesive zones terminate at non-convergence (presumed failure), while non-cohesive simulations terminate at average experimental strain.

Figure 13 shows a comparison of the model with cohesive zones (same curves as the ones labeled "COH" in Figure 12) against experimentally obtained data. One representative curve is chosen for each density. Overall, good agreement is evident. In the case of 95.5% r.d. model, artificially smaller neck curvatures had to be introduced to avoid neck impingement, resulting in a higher stress concentration and therefore weaker material behavior compared to experiments. It is notable that the 89% r.d. curve also shows a deviation between simulation and experiment. The reason for this is unclear; however, it should be noted that a small variation in tensile behavior naturally exists between different samples.

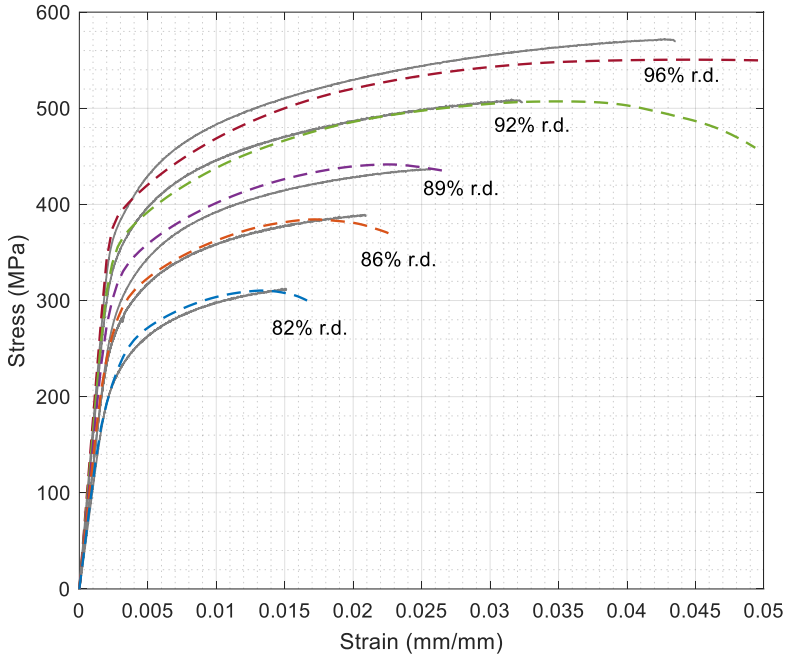

Figure 13: Comparison between simulated and experimental results. RVE model results with cohesive zones are shown as colored dashed lines, while representative experimental curves for each density are plotted as grey solid lines.

Quantitative comparison of the predicted and measured critical stress values is made in Paper D, showing very good agreement. In case of the total elongation and predicted fracture strains, a good agreement is observed for densities between 82%-89% r.d.. For higher densities, increasingly larger fracture strains are predicted by the model (as seen in Figure 12). This is attributed to the differences between the RVE and real microstructure, when it comes to the effect of density on pore size distribution. At higher densities, the distribution of pore size in the real material skews towards small pores with a few larger pores remaining. These are assumed to have a disproportionate effect on fracture behavior. On the other hand, the RVE represents an averaged microstructure with identical pores and thus cannot accurately capture limit strains when those are increasingly controlled by the largest defect.

One important issue in the context of damage development is to identify the locations where the damage starts to develop and propagate. The most likely scenario at failure is that cracks develop in a limited number of necks, leading to

catastrophic failure [44, 45]. Accordingly, numerical simulations were carried out with one, two and three active cohesive zones where failure is possible, initially at one density. The results are shown in Figure 14 for 86% r.d. and compared with the scenario where all 24 necks are allowed to fail (c.f. Figure 12).

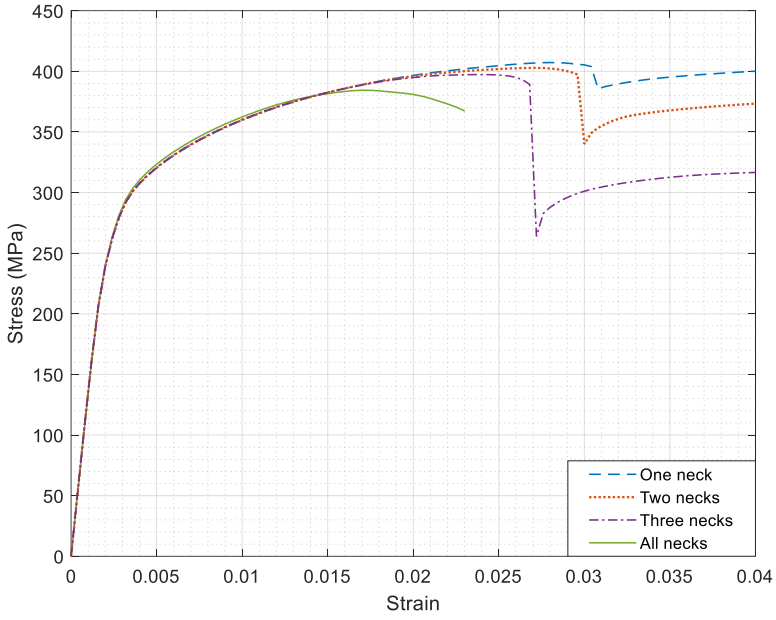

Figure 14: Simulation results with few cohesive zones at 86% r.d.. The dashed lines correspond to cases where one, two or three necks in the model are assigned cohesive properties with the rest having matrix material properties. The solid line shows the case when all necks have cohesive properties.

From the results in Figure 14 it is seen that both the failure load and strain are slightly dependent on the number of active (failing) necks, where the fracture load decreases when the number of active necks is increasing. Furthermore, the results indicate that softening behavior is significantly reduced when the number of damaged necks is limited. Adjusting the cohesive parameters to increase the brittleness of the material could lead to further elimination of the softening behavior.

It is clear that when damage initiates and leads to failure of a neck, a catastrophic load drop occurs. The simulation results show that after the load drop a load-carrying capacity is still present. This is, however, an artifact, as cohesive zones are not activated at the remaining necks, making complete separation impossible.

5 Conclusions and outlook

This thesis proposed and validated a modeling framework for porous sintered steels based on experimental measurements and observations. First, experimental measurements of mechanical properties at different densities were carried out, along with macroscopic shrinkage measurements. A mean-field sintering model was implemented with a new computational scheme. Sintering simulations were carried out incorporating mobility data from literature and from kinetic databases. The density-dependent shrinkage trend is captured by the model for higher-temperature sintering. Possible reasons for discrepancy were discussed. Lastly, the utility of the sintering model as an investigative or design tool is demonstrated via parametric studies. To simulate and predict stress-strain behavior, a mechanical RVE model is introduced, based on fcc unit cell geometry. The model is first calibrated for elasto-plastic behavior and shown to capture density dependence well. The effect of changing pore characteristics is investigated qualitatively. Next, cohesive zone modeling is implemented to capture fracture behavior. Investigations are performed to see the effect from a different number of cohesive zones. The overall fracture behavior is captured well by the RVE (peak stress, in particular), however challenges remain in predicting fracture strains at the highest densities considered.

The overall modeling framework is shown to be suitable for powder metals produced by press-and-sinter and relevant in understanding mechanistic effects on their microstructure and properties. This is achieved by capturing multiple linkages within the material system (as illustrated by Figure 15, where the linkages accounted for in the proposed framework are highlighted in blue and orange).

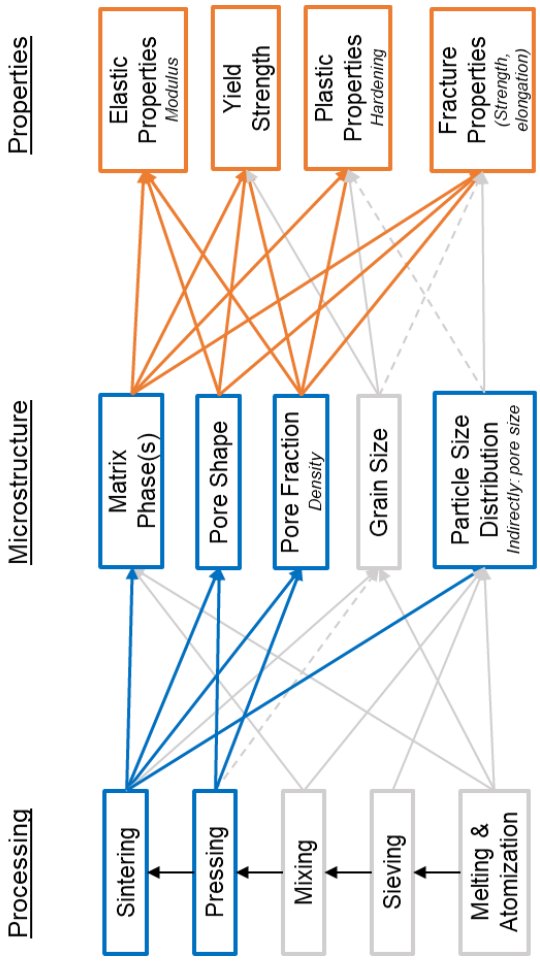

Figure 15: SDC for Astaloy® 85 Mo with 0.4%-0.6% C used in this study with boxes and arrows highlighted in blue representing aspects incorporated into the sintering model and in orange the micromechanical model.

Some challenges were also uncovered in making the framework predictive. Uncertainties in surface and grain boundary diffusion parameters, effects of particle shape and size distribution on shrinkage, as well as effects of pore size distribution on properties are all aspects that would need to be investigated and addressed to achieve better predictive ability. In this regard, some avenues for future work could include:

- Developing a method for obtaining more accurate data for surface and boundary diffusion. This could include, for example, drawing on first-principles or MD simulations or careful experimental investigations of

microstructure changes that could be used to calibrate these parameters in the model.

- Understanding the effects of realistic particle shape and particle size distribution on macroscopic shrinkage and how it could be accounted for in the sintering model.
- Parametric investigations into the cohesive zone model to achieve fracture behavior that is more representative of real materials. In particular, applying a statistical distribution to the cohesive parameters and understanding its effect on fracture.
- Extending the RVE model to fatigue predictions through the introduction of a damage parameter.
- Further exploration of the possible linkages between the sintering process and constitutive parameters in the mechanical model. This could involve the application of empirical models linking *e.g.* cohesive properties to neck growth or pore rounding due to the sintering process.

6 References

[1] E. Mosca, "Powder Metallurgy--Criteria for Design and Inspection," *Associazione Industriali Metallurgici-Metalmeccanici Affini,* 1984.

[2] O. Schenk, Y. Deng, A. Kaletsch, and C. Broeckmann, "Multiscale investigation of sintering kinetics of Astaloy 85Mo," *Powder Metallurgy,* vol. 67, no. 1, pp. 18-29, 2024-02-01 2024, doi: 10.1177/00325899231218543.

[3] H. Danninger, D. Spoljaric, and B. Weiss, "Microstructural features limiting the performance of P/M steels," *International journal of powder metallurgy,* vol. 33, no. 4, pp. 43-53, 1997.

[4] J. Pan, "Modelling sintering at different length scales," *International Materials Reviews,* vol. 48, no. 2, pp. 69-85, 2003-04-01 2003, doi: 10.1179/095066002225010209.

[5] H. Danninger, G. Jangg, B. Weiss, and R. Stickler, "Microstructure and mechanical properties of sintered iron. Pt. 1; Basic considerations and review of literature," *Powder Metallurgy International;(Germany),* vol. 25, no. 3, 1993.

[6] E. A. Olevsky, "Theory of sintering: from discrete to continuum," (in English), *Materials Science & Engineering R-Reports,* vol. 23, no. 2, pp. 41-100, Jun 30 1998, doi: Doi 10.1016/S0927-796x(98)00009-6.

[7] A. Hadrboletz and B. Weiss, "Fatigue behaviour of iron based sintered material: a review," *International Materials Reviews,* vol. 42, no. 1, pp. 1-44, 1997, doi: 10.1179/imr.1997.42.1.1.

[8] G. B. Olson, "Computational design of hierarchically structured materials," (in English), *Science,* vol. 277, no. 5330, pp. 1237-1242, Aug 29 1997, doi: DOI 10.1126/science.277.5330.1237.

[9] J. R. Rice and D. M. Tracey, "On the ductile enlargement of voids in triaxial stress fields∗," *Journal of the Mechanics and Physics of Solids,* vol. 17, no. 3, pp. 201-217, 1969, doi: 10.1016/0022-5096(69)90033-7.

[10] A. L. Gurson, "Continuum Theory of Ductile Rupture by Void Nucleation and Growth: Part I—Yield Criteria and Flow Rules for Porous Ductile Media," (in en), *Journal of Engineering Materials and Technology,* vol. 99, no. 1, pp. 2-15, 1977/01/01 1977, doi: 10.1115/1.3443401.

[11] V. Tvergaard, "On localization in ductile materials containing spherical voids," (in en), *International Journal of Fracture,* vol. 18, no. 4, pp. 237-252, 1982-04-01 1982, doi: 10.1007/BF00015686.

[12] J. B. Leblond and G. Perrin, "A self-consistent approach to coalescence of cavities in inhomogeneously voided ductile solids," *Journal of the Mechanics and Physics of Solids,* vol. 47, no. 9, pp. 1823-1841, 1999, doi: 10.1016/s0022-5096(99)00003-4.

[13] A. Benzerga, "Micromechanics of coalescence in ductile fracture," *Journal of the Mechanics and Physics of Solids,* vol. 50, no. 6, pp. 1331-1362, 2002, doi: 10.1016/s0022-5096(01)00125-9.

[14] V. Tvergaard and A. Needleman, "Effects of nonlocal damage in porous plastic solids," *International Journal of Solids and Structures,* vol. 32, no. 8-9, 1995/04/01, doi: 10.1016/0020-7683(94)00185-Y.

[15] T. W. J. De Geus, R. H. J. Peerlings, and M. G. D. Geers, "Fracture in multi-phase materials: Why some microstructures are more critical than others," *Engineering Fracture Mechanics,* vol. 169, pp. 354-370, 2017, doi: 10.1016/j.engfracmech.2016.08.009.

[16] W. A. Spitzig, R. E. Smelser, and O. Richmond, "The evolution of damage and fracture in iron compacts with various initial porosities," *Acta Metallurgica,* vol. 36, no. 5, pp. 1201-1211, 1988, doi: 10.1016/0001-6160(88)90273-8.

[17] F. Fritzen, S. Forest, T. Böhlke, D. Kondo, and T. Kanit, "Computational homogenization of elasto-plastic porous metals," *International Journal of Plasticity,* vol. 29, pp. 102-119, 2012, doi: 10.1016/j.ijplas.2011.08.005.

[18] P. Scholzen and M. Andersson, "Modelling Surface Densification Rolling of Powder Metal Gears," presented at the Euro PM2024, Malmö, 2024.

[19] J. D. Eshelby, "The determination of the elastic field of an ellipsoidal inclusion, and related problems," *Proceedings of the royal society of London. Series A. Mathematical and physical sciences,* vol. 241, no. 1226, pp. 376-396, 1957.

[20] H. Yuan, L. Zhang, and S. Ma, "Damage evolution and characterization for sintered powder metals with the varying porosity," *Engineering*

Fracture Mechanics, vol. 207, pp. 86-98, 2019, doi: 10.1016/j.engfracmech.2018.12.014.

[21] N. Chawla and X. Deng, "Microstructure and mechanical behavior of porous sintered steels," *Materials Science and Engineering: A,* vol. 390, no. 1, pp. 98-112, 2005/01/15/ 2005, doi: https://doi.org/10.1016/j.msea.2004.08.046.

[22] G. Straffelini and A. Molinari, "Evolution of tensile damage in porous iron," *Materials Science and Engineering: A,* vol. 334, no. 1, pp. 96-103, 2002/09/01/ 2002, doi: https://doi.org/10.1016/S0921-5093(01)01776-2.

[23] G. Straffelini, M. Benedetti, and V. Fontanari, "Damage evolution in sinter-hardening powder-metallurgy steels during tensile and fatigue loading," *Materials & Design,* vol. 61, pp. 101-108, 2014, doi: 10.1016/j.matdes.2014.04.027.

[24] E. Bernardo, A. Galan-Salazar, M. Campos, and J. M. Torralba, "A New Approach to Understand the Contribution of the Microstructure in the Fracture Behavior of Sintered Steels," *International Journal of Powder Metallurgy,* vol. 52, no. 2, 2016.

[25] H. Pan, S. H. Ko, and C. P. Grigoropoulos, "The solid-state neck growth mechanisms in low energy laser sintering of gold nanoparticles: A molecular dynamics simulation study," (in English), *Journal of Heat Transfer-Transactions of the Asme,* vol. 130, no. 9, Sep 2008, doi: 10.1115/1.2943303.

[26] A. M. Tahir, "Alloy element redistribution during sintering of powder metallurgy steels," KTH Royal Institute of Technology, 2014.

[27] K. Asp and J. Ågren, "Phase-field simulation of sintering and related phenomena – A vacancy diffusion approach," *Acta Materialia,* vol. 54, no. 5, pp. 1241-1248, 2006/03/01/ 2006, doi: https://doi.org/10.1016/j.actamat.2005.11.005.

[28] M. Braginsky, V. Tikare, and E. Olevsky, "Numerical simulation of solid state sintering," *International Journal of Solids and Structures,* vol. 42, no. 2, pp. 621-636, 2005, doi: 10.1016/j.ijsolstr.2004.06.022.

[29] E. A. Olevsky, V. Tikare, and T. Garino, "Multi-Scale Study of Sintering: A Review," *Journal of the American Ceramic Society,* vol. 89, no. 6, pp. 1914-1922, 2006, doi: 10.1111/j.1551-2916.2006.01054.x.

[30] A. Rajaei, Y. Deng, O. Schenk, S. Rooein, A. Bezold, and C. Broeckmann, "Numerical Modelling of the Powder Metallurgical Manufacturing Chain of High Strength Sintered Gears," *Chinese Journal of Mechanical Engineering,* vol. 34, no. 1, 2021, doi: 10.1186/s10033-021-00646-4.

[31] K. S. Hwang, R. M. German, and F. V. Lenel, "Analysis of Initial-Stage Sintering through Computer-Simulation," (in English), *Powder Metallurgy International,* vol. 23, no. 2, pp. 86-91, Apr 1991.

[32] S. G. Dubois, "Sintering of high surface area tantalum powder: simulation and experimental verification," Pennsylvania State University, 1995.

[33] J. Svoboda and H. Riedel, "New solutions describing the formation of interparticle necks in solid-state sintering," *Acta Metallurgica et Materialia,* vol. 43, no. 1, pp. 1-10, 1995, doi: 10.1016/0956-7151(95)90255-4.

[34] D. Bouvard and R. McMeeking, "Deformation of interparticle necks by diffusion-controlled creep," *Journal of the American Ceramic Society,* vol. 79, no. 3, pp. 666-672, 1996.

[35] F. Parhami, R. M. McMeeking, A. Cocks, and Z. Suo, "A model for the sintering and coarsening of rows of spherical particles," *Mechanics of Materials,* vol. 31, no. 1, pp. 43-61, 1999.

[36] C. L. Martin, L. C. R. Schneider, L. Olmos, and D. Bouvard, "Discrete element modeling of metallic powder sintering," *Scripta Materialia,* vol. 55, no. 5, pp. 425-428, 2006/09/01/ 2006, doi: https://doi.org/10.1016/j.scriptamat.2006.05.017.

[37] R. M. German, *Sintering theory and practice*. John Wiley & Sons, Inc., 1996.

[38] R. J. Bourcier, D. A. Koss, R. E. Smelser, and O. Richmond, "The influence of porosity on the deformation and fracture of alloys," *Acta Metallurgica,* vol. 34, no. 12, pp. 2443-2453, 1986/12/01/ 1986, doi: https://doi.org/10.1016/0001-6160(86)90147-1.

[39] R. Becker, "The effect of porosity distribution on ductile failure," *Journal of the Mechanics and Physics of Solids,* vol. 35, no. 5, pp. 577-599, 1987/01/01/ 1987, doi: https://doi.org/10.1016/0022-5096(87)90018-4.

[40] M. Andersson, "Finite Element Based Simulations of Mechanical Properties in Sintered Steels," presented at the Euro PM2019, Maastricht, 2019, EP1904346203.

[41] M. Andersson and M. Schneider, "A Finite Element Based Model Of The Influence Of Density On PM Mechanical Properties," presented at the Euro PM2021, 2021, EP215067614.

[42] T. Nagata, T. Takemasu, T. Koide, and N. Hirose, "Tooth Root Bending Stress Analysis of Pre-alloyed Sintered Steel Gears with Different Densities using FEM Model Considering Voids," *J. Japan Society of Powder and Powder Metallurgy,* vol. 63, no. 7, pp. 568-572, 2016, doi: 10.2497/jjspm.63.568.

[43] M. Doroszko and A. Seweryn, "A new numerical modelling method for deformation behaviour of metallic porous materials using X-ray computed microtomography," *Materials Science and Engineering: A,* vol. 689, pp. 142-156, 2017, doi: 10.1016/j.msea.2017.02.055.

[44] M. Kabátová, E. Dudrová, and A. S. Wronski, "Fracture micromechanics of static subcritical growth and coalescence of microcracks in sintered Fe–1·5Cr–0·2Mo–0·7C steel," *Powder Metallurgy,* vol. 49, no. 4, pp. 363-368, 2006-12-01 2006, doi: 10.1179/174329006x128313.

[45] J. M. Torralba, L. Esteban, E. Bernardo, and M. Campos, "Understanding the contribution of the microstructure in the fracture behaviour of sintered steels," *Powder Metallurgy,* vol. 57, no. 5, pp. 357-364, 2014, doi: 10.1179/1743290114Y.0000000119.